ICARUS 125, 245–260 (1997)
ARTICLE NO. IS965494

The Orbit of Charon

I. New Hubble Space Telescope Observations

DAVID J. THOLEN

Institute for Astronomy, University of Hawaii, 2680 Woodlawn Drive, Honolulu, Hawaii 96822
E-mail: tholen@ifa.hawaii.edu

AND

MARC W. BUIE

Lowell Observatory, 1400 W. Mars Hill Road, Flagstaff, Arizona 86001

Received December 12, 1994; revised March 27, 1996

The orbit of Charon has been determined from 60 images of the Pluto–Charon system acquired with the Hubble Space Telescope Wide Field and Planetary Camera between 1992 May 21 and 1993 August 18. The semimajor axis was found to be 19,636 ± 8 km, in good agreement with an older determination upon which mutual-event-based radius computations have relied, but significantly larger than two other recent determinations. Contrary to expectations based on the tidal evolution of the system, a surprisingly large eccentricity of 0.0076 ± 0.0005 was found, with the line of apsides aligned nearly along the line of sight from Earth. Approximately half of this apparent eccentricity could be due to offsets in the center of light from the center of body arising from surface albedo features on Pluto and Charon, which leaves a statistically significant portion unexplained. We propose that the remaining eccentricity is the result of a recent energetic impact. The remaining elements are generally consistent with previously determined values, though in the case of the inclination, the various determinations appear to have underestimated error bars. The system *GM* derived from our data is 981.5 ± 1.1 km^3 sec^{-2}. Some information on the Charon/Pluto mass ratio is present in the data, though our determination of $0.110^{+0.063}_{-0.056}$ does not improve on previous determinations, or resolve the discrepancy between them.

INTRODUCTION

The determination of absolute radii for Pluto and Charon from mutual event data relies on an accurate value for the semimajor axis of Charon's orbit. Recent determinations of the semimajor axis by Null *et al.* (1993) and Young *et al.* (1994) are smaller than the value found by Beletic *et al.* (1989), which had been the value most frequently used to scale mutual-event-based radii. The smaller radii that result from the use of the newer semimajor axis values produce larger discrepancies between some of the mutual-event-based radii (Tholen and Buie 1990, Reinsch *et al.* 1994) and stellar occultation determinations for the radius of Pluto (Millis *et al.* 1993) and a lower limit for the radius of Charon (Walker 1980, with a more recent reanalysis by Elliot and Young 1991).

In addition, a frequent assumption used in the analysis of data about this system is that it has completely tidally evolved. A match between the orbital period of Charon and the rotational period of Pluto is the most frequently cited observational evidence for complete tidal evolution, while theoretical arguments have been used to conclude that Charon's rotational period is also the same as the other two periods (Farinella *et al.* 1979). Although the mutual event data placed an upper limit of less than 10^{-3} on Charon's orbital eccentricity if the line of apsides was not aligned with the line of sight from Earth (Tholen and Buie 1990), the global upper limit of about 10^{-2} was substantially less useful in providing another observational constraint on the state of the system's tidal evolution (Tholen and Buie 1989). Fortunately, direct imaging is more sensitive to the eccentricity for orientations of the line of apsides that are along the line of sight. A combination of mutual event and direct imaging data would thus provide the tightest observational constraints on Charon's eccentricity.

The radii of Pluto and Charon, as determined from the modeling of mutual event data, also depend on the orientation of the orbit plane for Charon. Although these data can be used to measure the orientation, they do a considerably poorer job of determining the inclination than the longitude of the ascending node. It is far easier to determine the inclination by measuring the position angle of the major axis of the projected ellipse using direct imaging techniques. Given both the sensitivity of the mutual-event-

0019-1035/97 $25.00

based radii to Charon's inclination and the discrepancy with the stellar occultation results, we felt that fixing the inclination at a value obtained from direct imaging would be superior to allowing that parameter to float during the mutual event modeling. Unfortunately, the two values for the inclination published by Null *et al.* (1993) and Young *et al.* (1994) differ by 4.4 standard deviations, and both are significantly less than the value determined by Beletic *et al.* (1989) and the one derived from mutual event modeling in which the inclination was a free parameter (Tholen and Buie 1990).

Another annoying discrepancy between the results of Null *et al.* (1993) and Young *et al.* (1994) concerns the primary goal of their observations, namely the Charon/Pluto mass ratio, for which the formal difference is 4.8 standard deviations. Clearly, another independent result is needed.

For these reasons, we pursued a new determination of Charon's orbit using the facility offering the highest available angular resolution, namely the Hubble Space Telescope (HST). Fortunately, these goals could be accomplished using the same observations that had been planned to acquire separate rotational lightcurves for Pluto and Charon, so we were able to achieve several important goals using the same data. The lightcurve results are reported in a companion paper (Buie *et al.* 1997), while the astrometric results are the topic of this paper.

HISTORY

Our knowledge of Charon's orbit has been steadily improving since the satellite's discovery in 1978 (Smith 1978, Christy and Harrington 1978). The earliest orbit determinations were based on low angular resolution photographs of the system dating as far back as 1965 (Christy and Harrington 1978, Harrington and Christy 1980). The next major improvement became possible after the first speckle interferometric observations were made in 1980 (Bonneau and Foy 1980, Harrington and Christy 1981). More extensive speckle observations spanning a full orbit were instrumental in providing yet another improvement (Baier and Weigelt 1987, Tholen 1985), though the disagreement with other speckle observations (Bonneau and Foy 1980, Hege *et al.* 1982, Hetterich and Weigelt 1983, Hege and Drummond 1984) led us to suspect the accuracy of their image scale and position angle calibrations. The semimajor axis that we had adopted for purposes of modeling the radii of Pluto and Charon using mutual event data, 19,640 ± 320 km, was derived from a well-calibrated speckle-based orbit determination by Beletic *et al.* (1989).

Between 1985 and 1990, photometric observations of mutual events between Pluto and Charon were acquired, with annual improvements being made in the period, mean longitude, ascending node, and inclination of Charon's orbit (see Tholen and Buie 1988 and references therein). The mutual event data could not be used to determine the semimajor axis of the orbit directly. Although the imposition of limits on the albedos of the two bodies could have been used to produce similar limits on the semimajor axis, such limits would have been far cruder than any of the semimajor axes previously published.

Following the launch of the Hubble Space Telescope, high angular resolution imaging became possible, and an improved semimajor axis resulted from observations made over half an orbit (Null *et al.* 1993), though their primary goal was to measure the Charon/Pluto mass ratio by observing the barycentric wobble of the system. A similar project utilizing CCD imaging from a ground-based site with good seeing and data covering a full orbit produced a comparable result for the semimajor axis (Young *et al.* 1994). Because of the short time interval spanned by their observations, it was not possible to perform a solution for the orbital period that represented any improvement over previous results. Neither set of observations was able to detect any orbital eccentricity at a significant level.

OBSERVATIONS

Sixty images of the Pluto–Charon system were obtained between 1992 May 21 and 1993 August 18, as shown in Table I. For reasons of consistency and to minimize the complexity of the reductions, all observations were made with the same CCD chip (P6) of HST's Wide Field and Planetary Camera. The observing strategy called for exposures to be made in groups of four, with two consecutive exposures made within minutes of each other to guard against the loss of useful data due to cosmic ray strikes on the images, and a second pair of exposures made several hours later, after Pluto had moved a significant fraction of the Planetary Camera's single-chip field of view. Our intent was to obtain all images while Pluto was near a field star; unfortunately, four groups of observations were lost due to an opposition pointing constraint that was imposed following a spacecraft safing event. When rescheduling those observations, we were not able to find suitable field stars close to the system at the times when Charon was near the specific orbital longitudes intended to be covered by the lost observations. Because the longitude coverage was more important to us, we chose to observe without a nearby field star (as indicated by dashes in Table I).

The F555W filter was used for the majority of the observations. On two occasions, the exposure groups were obtained through both the F555W and F439W filters. So although most of the observations came in groups of four, two came in groups of eight; thus the 60 observations represent a total of 13 substantially different epochs. For purposes of the astrometry, we did not distinguish between the two filters.

TABLE I

Image Centroids, Roll Angles, Relative Positions, and Orbit Solution Residuals

Exposure	Pluto		Charon		Field star					Residuals	
midtime (JDT)	x	y	x	y	x	y	V_3 (°)	Sep. (")	P. A. (°)	Sep. (")	P. A. (°)
2448763.5719036	165.07	304.20	159.79	319.49	553.10	483.84	343.51	0.7140	1.61	+0.0007	+0.04
2448763.5760703	169.21	306.57	163.95	321.76	547.04	479.74	343.51	0.7095	1.66	−0.0014	+0.01
2448763.8399592	425.66	434.33	420.52	445.31	294.33	349.87	342.77	0.5351	6.90	−0.0008	−0.40
2448763.8441258	429.57	438.38	424.39	449.36	288.61	347.41	342.77	0.5359	7.08	+0.0030	−0.35
2448771.9462093	463.55	131.29	471.51	113.95	294.29	639.69	324.77	0.8422	168.48	+0.0025	+0.12
2448771.9503759	466.21	134.21	474.25	116.76	289.77	634.17	324.77	0.8480	168.56	+0.0067	+0.15
2448771.9554106	466.79	137.58	474.71	120.26	280.18	626.77	324.77	0.8406	168.39	−0.0028	−0.07
2448771.9616606	471.18	141.84	479.14	124.53	273.24	619.87	324.77	0.8409	168.51	−0.0049	−0.02
2448772.2151329	667.13	322.40	676.87	303.95	82.27	444.94	324.32	0.9209	171.20	+0.0001	+0.07
2448772.2213829	672.44	326.94	682.16	308.40	75.26	436.66	324.32	0.9240	171.04	+0.0021	−0.16
2448772.2267648	680.31	331.98	690.15	313.52	72.97	431.48	324.32	0.9233	171.43	+0.0004	+0.19
2448772.2309315	683.44	335.21	693.27	316.74	68.26	426.97	324.32	0.9235	171.39	−0.0002	+0.11
2448776.4524593	321.82	56.21	311.24	66.43	416.31	723.14	317.97	0.6493	3.01	+0.0025	−0.12
2448776.4566260	324.53	59.22	314.01	69.41	412.13	720.08	317.97	0.6465	2.93	+0.0023	−0.27
2448776.7031537	493.33	245.54	484.79	251.91	250.25	542.77	317.65	0.4703	9.98	+0.0008	+0.35
2448776.7073204	495.45	248.46	486.98	254.80	245.77	536.90	317.65	0.4670	9.88	+0.0008	+0.10
2448856.4219084	423.49	697.30	435.62	695.80	263.65	103.03	282.50	0.5395	184.50	−0.0033	+0.10
2448856.4260751	424.73	695.26	436.81	693.76	260.31	102.81	282.50	0.5373	184.47	−0.0025	−0.02
2448856.6899640	530.55	571.07	538.30	571.37	156.85	230.91	282.43	0.3423	193.70	−0.0010	−0.30
2448856.6941306	531.76	569.11	539.46	569.46	153.48	230.78	282.43	0.3402	194.08	+0.0001	−0.15
2448884.0205198	89.01	398.64	69.28	401.62	687.12	402.37	271.26	0.8807	351.72	−0.0022	−0.01
2448884.0246864	92.10	395.09	72.36	398.04	686.18	404.17	271.26	0.8810	351.81	−0.0024	+0.04
2448884.3503809	282.67	65.63	262.87	67.66	513.48	692.47	271.26	0.8785	354.45	−0.0049	−0.13
2448884.3545476	285.45	61.62	265.67	63.66	512.34	694.59	271.26	0.8777	354.42	−0.0052	−0.20
2448999.6837153	551.53	181.65	567.91	175.30	290.62	618.06	112.29	0.7754	0.15	+0.0026	+0.13
2448999.6878819	553.13	185.71	569.50	179.42	289.11	616.52	112.29	0.7741	0.32	+0.0030	+0.23
2449000.0857986	700.84	568.11	713.04	565.46	140.78	231.73	112.16	0.5510	8.95	−0.0015	−0.01
2449000.0899653	701.91	572.07	714.11	569.48	139.32	230.32	112.16	0.5505	9.22	+0.0007	+0.11
2449011.8219098	476.00	111.19	494.50	102.90	375.91	721.71	106.78	0.8948	351.69	−0.0032	+0.12
2449011.8260765	476.82	114.90	495.34	106.67	375.78	719.20	106.78	0.8945	351.87	−0.0037	+0.24
2449012.4739932	672.82	594.52	689.60	589.92	171.03	231.02	106.78	0.7680	0.50	−0.0025	+0.05
2449012.4781598	673.58	598.09	690.39	593.56	171.28	230.01	106.78	0.7684	0.75	−0.0001	+0.23
2449138.9469111	68.97	418.68	63.45	434.23	771.60	350.61	324.78	0.7283	343.37	+0.0005	0.00
2449138.9510777	72.18	421.13	66.61	436.67	765.51	346.85	324.78	0.7286	343.55	−0.0015	+0.09
2449138.9561124	72.29	424.33	66.73	440.02	754.56	340.73	324.78	0.7347	343.34	+0.0017	−0.20
2449138.9623624	77.22	428.19	71.55	443.98	747.47	333.86	324.78	0.7405	343.58	+0.0040	−0.08
2449139.2151402	288.67	614.54	281.95	632.69	543.45	153.33	328.34	0.8543	347.71	−0.0011	+0.10
2449139.2213902	293.82	618.57	287.02	636.80	534.10	147.79	328.34	0.8588	347.84	+0.0011	+0.16
2449139.2267722	302.07	622.39	295.30	640.59	530.87	143.04	328.34	0.8571	347.79	−0.0026	+0.04
2449139.2309388	305.49	625.16	298.68	643.42	526.21	138.69	328.34	0.8602	347.84	−0.0010	+0.02
2449155.0809390	312.28	71.31	324.27	57.50	522.88	688.22	305.82	0.8072	165.83	+0.0037	−0.17
2449155.0851057	314.49	74.44	326.52	60.61	520.21	682.37	305.82	0.8091	165.89	+0.0036	−0.18
2449155.3489946	454.50	270.91	468.92	256.38	378.83	491.30	305.62	0.9036	169.45	+0.0040	−0.04
2449155.3531612	456.78	274.01	471.13	259.47	376.93	485.33	305.62	0.9017	169.29	+0.0011	−0.24
2449174.3045306	144.02	274.20	158.84	262.84	—	—	295.50	0.8242	167.08	+0.0003	−0.01
2449174.3086972	145.79	275.90	160.65	264.44	—	—	295.50	0.8283	166.91	+0.0027	−0.23
2449174.6941139	302.78	473.11	320.30	461.76	—	—	295.35	0.9214	171.46	−0.0033	−0.15
2449174.6982806	304.98	474.72	322.60	463.38	—	—	295.35	0.9249	171.63	−0.0003	−0.03
2449212.1864754	469.50	356.47	480.04	349.28	—	—	284.64	0.5632	159.39	−0.0029	+0.13
2449212.1927254	469.69	356.48	480.34	349.24	—	—	284.64	0.5684	159.48	−0.0019	+0.05
2449213.6531420	471.37	354.08	488.89	349.54	—	—	284.29	0.7988	178.81	+0.0022	+0.18
2449213.6593920	471.32	354.04	488.82	349.50	—	—	284.29	0.7980	178.80	+0.0040	+0.08
2449214.8573087	472.74	353.47	471.12	357.88	—	—	284.00	0.2074	303.22	+0.0025	+2.67
2449214.8642532	472.76	353.46	471.31	357.87	—	—	284.00	0.2049	301.25	−0.0037	−0.67
2449215.3211976	473.20	354.91	463.32	361.82	—	—	283.90	0.5322	337.98	+0.0022	−0.09
2449215.3878643	473.17	354.92	462.24	362.05	—	—	283.90	0.5760	339.83	+0.0006	−0.09
2449217.7330032	465.00	380.57	460.39	378.34	—	—	283.32	0.2260	38.18	−0.0005	−0.93
2449217.7392532	465.03	380.55	460.63	378.38	—	—	283.32	0.2165	38.62	−0.0063	−1.53
2449218.0677254	465.27	381.57	466.81	377.08	—	—	283.24	0.2095	121.22	−0.0058	−1.93
2449218.0739754	465.75	381.51	467.42	377.01	—	—	283.24	0.2119	122.65	−0.0069	−1.62

The exposure times were 30 sec for all images taken through the F555W filter and 120 sec for the F439W filter. The telescope was pointed at the midpoint between the Pluto–Charon system and the field star, and tracking was at half the rate of motion for the system, thereby smearing both the field star and Pluto–Charon slightly. The maximum amount of smearing was less than 0.020 arcsec, however, which is less than one-half pixel.

DATA REDUCTION

Details of the image processing are provided in the companion paper (Buie *et al.* 1996). Centroiding was performed on the CLEANed images after convolution with a Gaussian image profile using the center-of-light technique. Note that Pluto represents a resolved source for the Planetary Camera, whereas the diameter of Charon is approximately equal to the size of one pixel. Although the nearby field star would normally represent a point spread function, recall that the tracking rate chosen for these observations was half the rate of motion for the system, thereby smearing the images of the field star, Pluto, and Charon by equal amounts.

For 54 of the images, the centroiding procedure was accomplished using a 3-pixel radius (0.26 arcsec diameter) aperture centered on each object (see Buie and Bus 1992 for more discussion of the technique); however, for the six images obtained with Pluto and Charon near minimum separation, contamination from the other object caused this centroiding procedure to fail. For these, it was necessary to manually control the centering of the object in the aperture before computing the center of light. When the final weighted orbit solutions were performed, these six observations were assigned uncertainties two and one half times larger than the others, a number that was determined from their relative scatter in preliminary orbit solutions.

Corrections for field distortion were accomplished using the METRIC routine (December 1992 version) provided in the Space Telescope Science Data Analysis Software (STSDAS) package. Figure 1 shows the corrected positions of Pluto as small dots, with the tails representing the size and direction of the correction, but exaggerated by a factor of 2 to make them easier to see. The maximum correction was 5.1 pixels, but the average correction was only 3.0 pixels. Note that the optical axis of HST falls near, but not precisely on, pixel (0,0). For purposes of the orbit solution for Charon, however, we are interested in the positional shift of Charon relative to Pluto. Because of the close proximity of Charon to Pluto, both objects received nearly the same absolute shift. The largest relative shift was only 0.2 pixel, with the average correction being 0.1 pixel (Fig. 2). Note from these diagrams that the Pluto–Charon system appeared all over the CCD, and the field distortion corrections for the relative positions are in random directions, thus we expect any errors that might be present in the field distortion model to average out, rather than producing a systematic error in the orbit solution.

We did not attempt to derive our own field distortion model, given that the ± 0.9 arcsec motion of Charon is about an order of magnitude larger than the ± 0.1 arcsec barycentric wobble of Pluto (see Null *et al.* 1993 for a more extensive discussion of field distortion problems), and we were using images with approximately half the image scale of those used for the wobble measurements, yielding a total motion about 20 times larger in term of pixels. The error in the field distortion model would need to exceed 50% to produce an error larger than the typical centroiding uncertainty of 0.05 pixel for Pluto and Charon.

CALIBRATION

The Pluto–Charon separation and position angle depend on knowledge of the telescope image scale and spacecraft roll angle, which are used to convert the measured x and y (that is, the CCD column and row) values for the image centroids to separations in arcsec and position angle relative to some adopted reference frame, which in this case was the mean equator and FK5 equinox of J2000.0.

Image scale. The image headers provided by the Space Telescope Science Institute (STScI) indicated an image scale of 0.04414 arcsec pixel^{-1} for the distortion-corrected field. We were able to check this value by using the 22 pairs of frames on which a field star was present. The JPL ephemeris DE245 was used to determine the spherical coordinates of Pluto for each observation midtime. The motion in arcseconds for a given pair of frames was determined by computing the great circle distance between the corresponding pair of DE245 positions. The motion of Pluto in pixels was determined by shifting the origin of the second frame of a pair by the difference in the position of the field star, rotating the second frame by the difference in roll angle, and then computing the distance between the two locations for Pluto.

Because the observing strategy called for two consecutive exposures within minutes of each other, and another two exposures several hours later, we had four exposures containing the same field star with which to work. The image scale could be computed by pairing the first exposure with either the third or fourth exposure of a group. Because the choice is arbitrary, we computed the image scale both ways (see Table II, where the uncertainties are shown directly above each value in units of the least significant digit). The weighted mean image scale was found to be 0.0441385 ± 0.0000058 arcsec pixel^{-1}, with the weighting determined from the inverse square of the individual uncertainties. This approach assumes that the centroiding errors are approximately the same for each frame, so the longer the arc, the smaller the relative error in the length

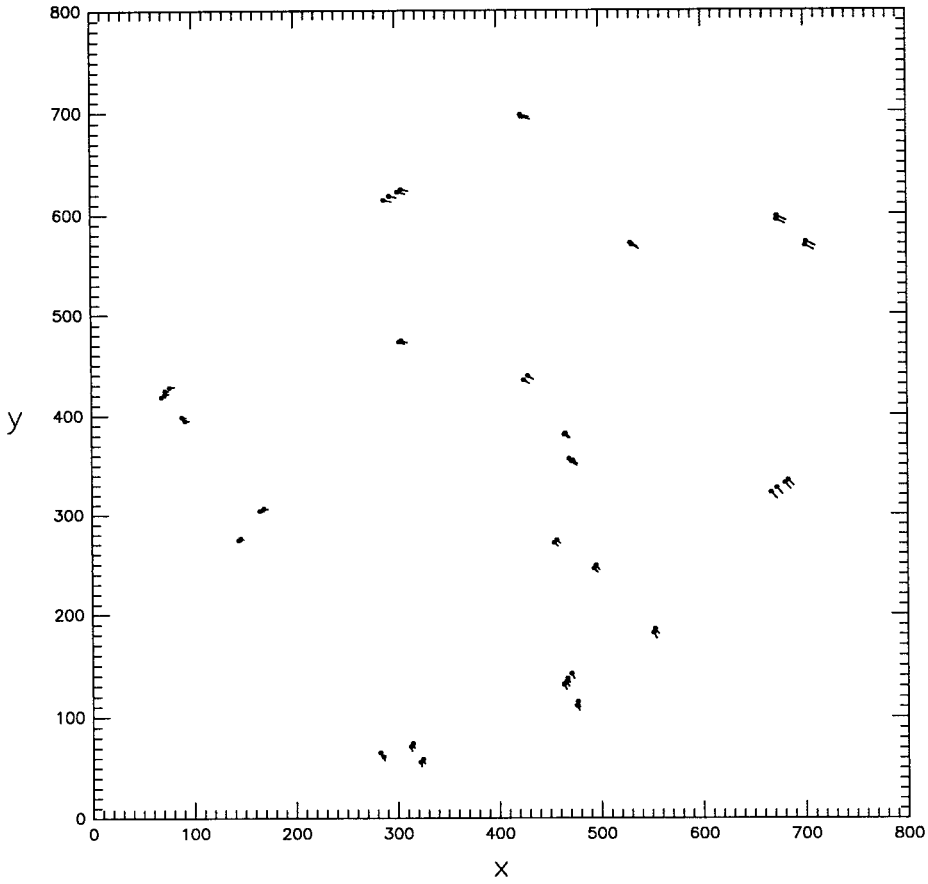

FIG. 1. Absolute field distortion map for P6. The dots represent the corrected positions of Pluto on the P6 CCD of the Wide Field and Planetary Camera, and the tails represent the direction and size of the correction. The lengths of the tails have been exaggerated by a factor of 2 to make them easier to see.

of that arc. Given that the various field stars have different brightnesses and some of their images were saturated, this assumption may not be very good. However, the mean image scale when all determinations were given equal weight was 0.044135 arcsec pixel^{-1}, which is well within the uncertainty of the weighted mean, which we decided to adopt. The adopted image scale is also entirely consistent with the STScI determination. The potential systematic error due to the uncertainty in the image scale determination is therefore a little more than one part in ten thousand, which for Charon's orbit amounts to less than 2.6 km.

Position angle. The position angle of Charon relative to Pluto is measured from J2000.0 north on the plane of the sky, positively to the east. The direction of north relative to the CCD columns on the P6 chip is provided by the spacecraft roll angle and a small offset between the V_3 axis and the CCD columns. The roll angle for each observation is shown in Table I, and the offset was determined by STScI to be $-0.880°$. The accuracy of the roll angle depends on the accuracy of the positions in the Guide Star Catalog (GSC) for the particular pair of stars utilized during the observations. Assuming an uncertainty in the position of one guide star relative to another of about 0.5 arcsec (Russell *et al.* 1990), and given the 730 arcsec distance between the center of the Fine Guidance Sensor and the optical axis, where the Planetary Camera is located, the typical uncertainty in the roll angle would be about 0.04°. Because the GSC errors will tend to be random, so will the errors in the roll angle of the spacecraft. Although individual observations may suffer from a larger roll angle error, our orbit determination benefits from the use of 24 different pairs of guide stars, so they should tend to reduce the noise in the inclination (which is the orbital parameter most directly coupled to the spacecraft roll angle) caused by GSC positional errors to slightly less than 0.01°.

A possible source of systematic error could arise from the $-0.880°$ offset of the CCD columns from the V_3 axis. Fortunately, using our knowledge of Pluto's motion from DE245 and techniques similar to those described for our

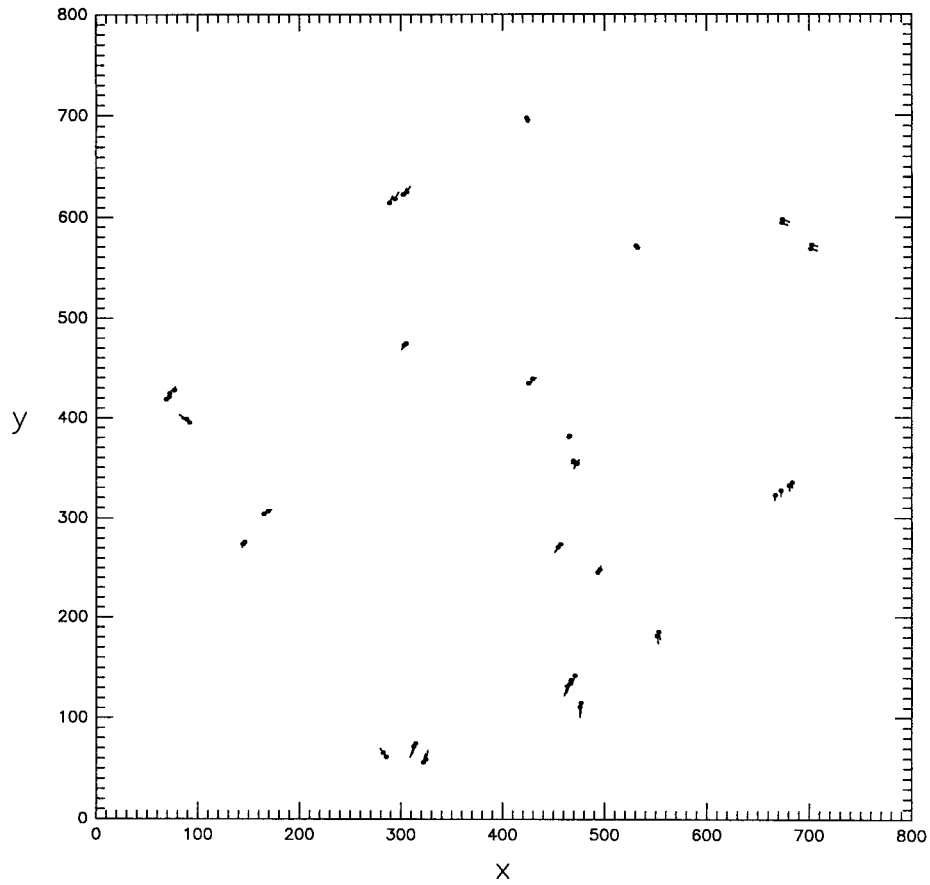

FIG. 2. Relative field distortion map for P6. The dots represent the corrected positions of Pluto on the P6 CCD of the Wide Field and Planetary Camera, and the tails represent the direction and size of the correction in the position of Charon relative to Pluto. The lengths of the tails have been exaggerated by a factor of 50 to make them easier to see.

determination of the image scale, we were able to independently compute the offset angle as $-0.9513° \pm 0.0075°$, as shown in Table II. This result has been more recently described as "consistent" with the STScI $-0.880°$ result, though we had originally been led to believe that their value was accurate to a few thousandths of a degree. The 0.0075° uncertainty is also consistent with what we expected after combining the results from 22 pairs of observations, each with a roll angle uncertainty of about 0.04°, but the 0.0075° uncertainty is about an order of magnitude smaller than the difference between our $-0.9513°$ value and the STScI $-0.880°$ value.

Fourteen of our images show pairs of field stars. To provide a partial check on STScI's roll angle computation, the position angle of one star relative to the other was computed for each of these 14 images. Although the baseline distance between field stars is much smaller than for the Planetary Camera and Fine Guidance Sensor combination, our centroiding errors are much smaller than the positional errors in the GSC, so it is possible to determine a change in the position angle to about the same level of accuracy as the roll angle and to compare these differences with the change in the roll angle. The largest peak-to-peak difference seen was 0.07°, and that was for two stars separated by only 5.3 arcsec. Adopting a centroiding error of about 0.005 arcsec (about 0.1 pixel) for the stars, the position angle in this case should be known to about 0.05°, which is consistent with the difference seen. No discrepancies in the roll angle differences were noted.

ORBIT SOLUTION

The procedure used to solve for the orbit of Charon was virtually identical to that used for the speckle observations reported by Beletic *et al.* (1989). The principal difference is that we used the J2000.0 reference frame rather than the B1950.0 frame used previously. Additional details are provided in the Appendix. The resulting orbital elements are shown in Table III, the orbit is plotted in Fig. 3, and the residuals are shown in Fig. 4 (in rectangular coordinates), as well as tabulated in Table I (in polar coordinates). The residuals for all but the six observations near minimum

TABLE II
HST Planetary Camera Image Scale and Position Angle Offset Calibration

Date (UT)	image scale (arcsec pixel^{-1})				position angle offset (°)			
	1-3 pairing	2-4 pairing	1-4 pairing	2-3 pairing	1-3 pairing	2-4 pairing	1-4 pairing	2-3 pairing
1992 May 21	30 0.044154	30 0.044190	29 0.044169	31 0.044175	39 −0.945	39 −0.959	38 −1.004	40 −0.898
1992 May 29 (F555W)	29 0.044144	29 0.044084	29 0.044114	30 0.044114	38 −0.962	38 −0.965	37 −1.000	39 −0.926
1992 May 29 (F439W)	32 0.044205	32 0.044114	31 0.044163	33 0.044156	42 −0.926	42 −0.868	41 −0.897	43 −0.897
1992 June 2-3	35 0.044136	35 0.044161	34 0.044162	36 0.044134	45 −0.931	45 −0.974	44 −0.977	46 −0.927
1992 August 21-22	52 0.044113	52 0.044113	52 0.044155	53 0.044071	68 −0.957	68 −0.960	67 −0.893	69 −1.028
1992 September 18	24 0.044106	24 0.044107	24 0.044091	24 0.044122	31 −0.948	31 −0.940	31 −0.981	32 −0.906
1993 January 12	21 0.044143	21 0.044160	21 0.044154	21 0.044150	27 −0.960	27 −0.989	27 −0.992	28 −0.957
1993 January 24	17 0.044147	17 0.044147	16 0.044135	17 0.044159	21 −0.958	21 −0.961	21 −0.996	22 −0.923
1993 May 31 (F555W)	29 0.044162	29 0.044135	29 0.044159	30 0.044138	38 −0.906	38 −0.942	37 −0.907	39 −0.943
1993 May 31 (F439W)	32 0.044156	32 0.044114	31 0.044149	33 0.044121	42 −0.930	42 −0.978	41 −0.932	43 −0.976
1993 June 16	36 0.044073	36 0.044101	35 0.044102	36 0.044070	46 −0.906	46 −0.973	45 −0.971	47 −0.907
	61 wtd. mean = 0.0441385		58 wtd. mean = 0.0441386		75 wtd. mean = −0.9512		84 wtd. mean = −0.9514	

separation average to only 0.0024 arcsec, with the remaining six showing an average residual of 0.0060 arcsec. For purposes of plotting the orbit in Fig. 3, the geometry of the system has been adjusted to the orbit centered on 1993 February 22, which removes virtually all of the additional scatter caused by the changing sub-Earth latitude and topocentric distance during the 15 months spanned by the observations.

The adopted orbit is based on a solution in which all 60 observations were used but were assigned unequal weight. The six observations closest to minimum separation were assigned uncertainties 2.5 times larger than for the other observations, commensurate with the residuals determined from preliminary orbit solutions. Weights are based on the inverse square of the assigned uncertainties. This solution is shown in the leftmost column of orbit solutions in Table III.

To assess the effect that the weighting procedure had on the solution, a second solution was performed in which all 60 observations were assigned the same weight, with the resulting elements shown in the second column of orbit solutions in Table III. There is no significant change in the orbit, with all differences from the adopted orbit being less than 1.5 standard deviations.

Because the six observations closest to minimum separation show Charon to be photometrically contaminated with light from Pluto (see the companion paper by Buie *et al.* 1997), and because the Charon centroids for these observations show systematic displacement toward Pluto, a third solution was performed in which these six observations

TABLE III
Orbit Solutions (Mean Equator and Equinox of J2000.0, Epoch JDT 2449000.5 = 1993 January 13.0 TT)

	unequal weight (all 60 obs.)	equal weight (all 60 obs.)	equal weight (54 obs.)	albedo model (Pluto only)	albedo model (Pluto and Charon)
semimajor axis (km)	19636 ± 8	19639 ± 8	19635 ± 7	19637 ± 8	19666 ± 8
eccentricity	0.0076 ± 0.0005	0.0079 ± 0.0005	0.0075 ± 0.0006	0.0030 ± 0.0005	0.0044 ± 0.0005
inclination (deg)	96.163 ± 0.032	96.168 ± 0.029	96.163 ± 0.027	96.169 ± 0.032	96.151 ± 0.032
ascending node (deg)	222.993 ± 0.024	223.039 ± 0.020	222.980 ± 0.031	222.999 ± 0.024	222.961 ± 0.024
long. periapsis (deg)	219.1 ± 2.2	216.3 ± 2.2	220.0 ± 2.3	219.2 ± 5.8	215.0 ± 3.6
mean longitude (deg)	32.875 ± 0.047	32.908 ± 0.046	32.871 ± 0.048	32.793 ± 0.047	32.800 ± 0.047
period (days)	6.387223 ± 0.000017	6.387252 ± 0.000023	6.387210 ± 0.000017	6.387266 ± 0.000017	6.387254 ± 0.000017
GM (km^3 s^{-2})	981.5 ± 1.1	981.9 ± 1.2	981.2 ± 1.1	981.6 ± 1.1	985.9 ± 1.1

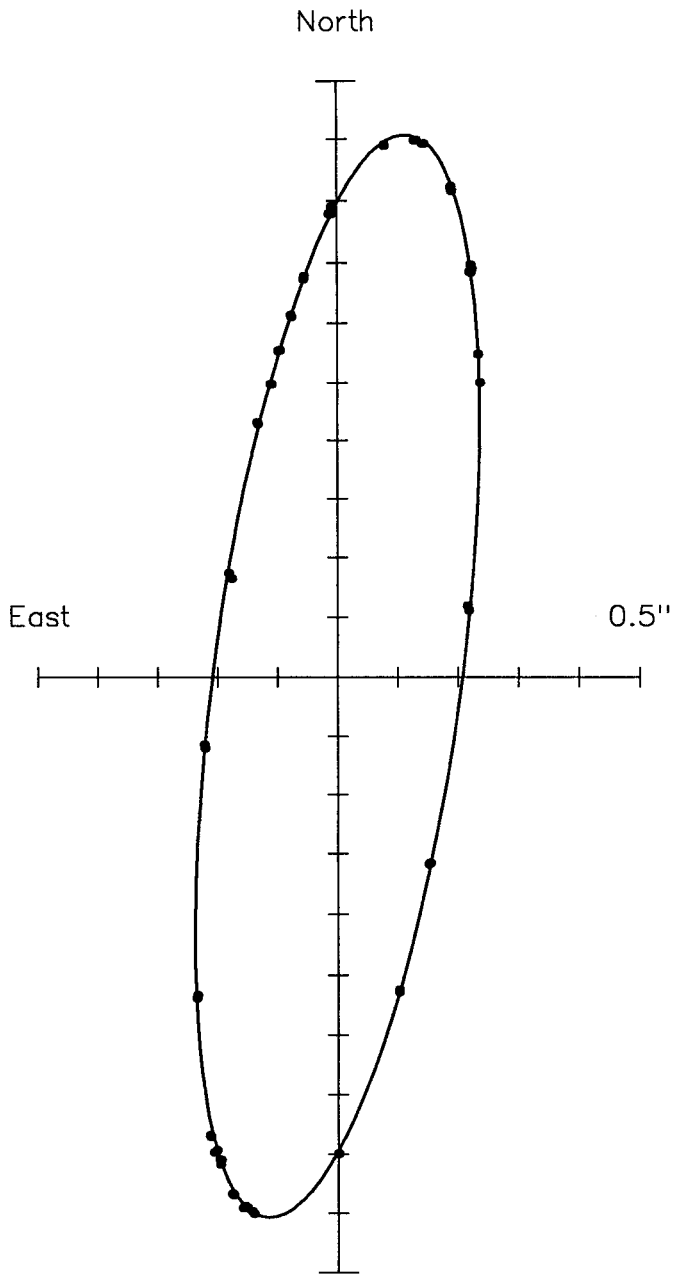

FIG. 3. The orbit of Charon. The dots represent the observations, and the solid curve represents the fitted orbit. To minimize the scatter produced by the varying sub-Earth latitude and topocentric distance during the fifteen months spanned by the observations, the data have been corrected to the single orbit interval centered on the epoch 1993 February 22. The orbital angular momentum vector points roughly toward the west, and the eastern portion of the orbit passes on the near side of Pluto.

were removed. We had initially speculated that because these observations fell the closest to periapsis and apoapsis, they might be dominating the solution for the eccentricity. The third column of orbit solutions in Table III shows this speculation to be unfounded. The eccentricity persists even when the contaminated observations are removed from the solution.

For purposes of the three preceding orbit solutions, the centroids derived from the HST images were assumed to represent the centers of the two bodies. Pluto, of course, is known to have a highly contrastive surface, so its surface albedo distribution can be expected to produce an offset between the center of body and the center of light. The evidence for surface contrast on Charon is much weaker. The accompanying paper by Buie *et al.* (1997) demonstrates that Charon has little rotational lightcurve variation (about 0.08 mag), though a difference in albedo between hypothetically uniform northern and southern hemispheres would not produce any rotational variation, yet could produce a significant latitudinal offset in the center of light from the center of body. The best global surface albedo maps that are available at the time of this writing were derived from a combination of rotational lightcurve and mutual event observations by Buie *et al.* (1992; note that Young and Binzel 1993 modeled only the eclipsed hemisphere of Pluto, and Reinsch *et al.* 1994 did not model Charon), though only one hemisphere of each object is constrained by mutual event data. The nonfacing hemisphere on each object is constrained primarily by the rotational lightcurve data of the system, and the maximum entropy technique used by Buie *et al.* (1992) tends to make Pluto and Charon look similar in the absence of data that show otherwise. The importance of the individual lightcurves presented in the accompanying paper should be readily apparent.

Two additional orbit solutions were performed using model values for the center-of-body to center-of-light (hereafter abbreviated COB–COL) offsets. The first of these solutions assumed that Charon has a reasonably uniform surface albedo distribution, as suggested by its small rotational lightcurve variation, such that there is no offset between the center-of-body and the center-of-light on Charon. The COB–COL offsets for Pluto were computed using the geometry of the system for the time of each HST observation and the maximum entropy surface albedo model for Pluto (Buie *et al.* 1992). Note that this albedo model was derived using an older orbit for Charon, so there is a slight internal inconsistency in applying these older results to the newer orbit solutions. Also, this model does yield a nonuniform Charon; thus the resulting surface albedo model for Pluto would certainly be different if Charon had been constrained to be uniform, as assumed for this particular orbit solution. Nevertheless, given that the albedo model is only an approximation to reality, the use of this model is sufficient to estimate the potential size of the effect that Pluto's surface albedo distribution has on the orbit solution.

The fourth column of orbit solutions in Table III shows

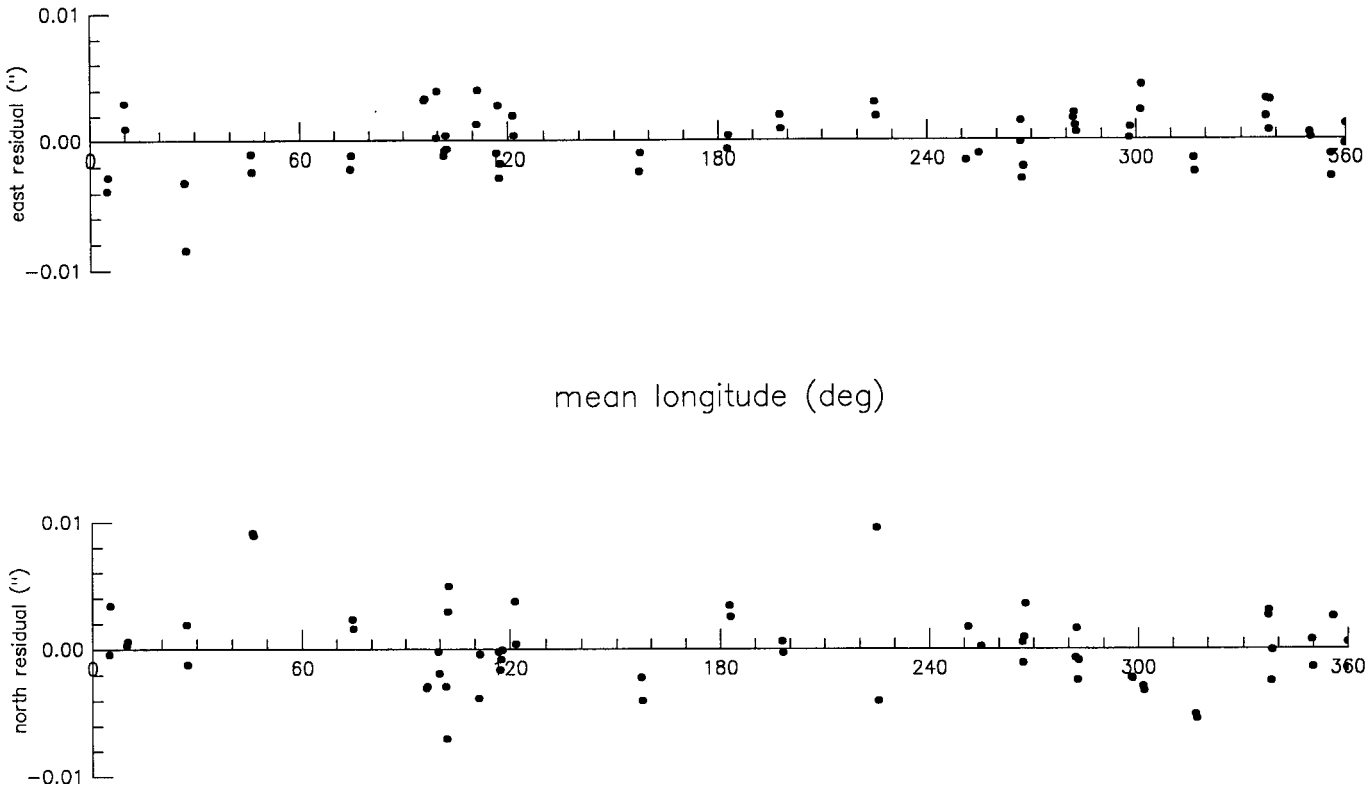

FIG. 4. Orbit solution residuals. The top plot shows the east residual in arcseconds, while the bottom plot shows the north residual in arcseconds. Except for the six observations that fall the closest to minimum separation (near 27°, 46°, and 225° mean longitude), the average residual is 0.0024 arcsec. The remaining six observations show an average residual of 0.0060 arcsec.

the effect of COB–COL offsets on Pluto only. Most of the orbital elements are affected only slightly, but the eccentricity was reduced by more than half, yet remains nonzero at a highly significant level.

The final orbit solution incorporates COB–COL offsets for both Pluto and Charon. Because the maximum entropy model tends to make Pluto and Charon look similar, in the absence of data that show otherwise, the COB–COL offsets tend to be in the same direction at longitudes away from where the mutual event data constrain the surface albedo distributions. We expected this partial "cancelling-out" effect to bring the eccentricity back up, and the last column of orbit solutions in Table III shows this expectation to be correct.

Although not shown here, a solution in which the eccentricity was forced to be zero increased the reduced χ^2 statistic by a factor of 1.9, which provides yet another indication of the reality of the eccentricity present in these data.

One other effect that we investigated was the field distortion correction provided by the METRIC routine. An orbit solution performed on raw, uncorrected data showed an increase of 24% in the average residual, with fairly significant changes in some of the orbital elements. The semimajor axis, for example, increased to 19,719 ± 11 km. Because the size of the relative correction between Pluto and Charon was much smaller than the absolute correction, the effect of METRIC's corrections was even more substantial for the image scale determination, for which the scatter doubled in size. Although the field distortion model used by METRIC may not be optimum, we are convinced that it is far better than using the raw, uncorrected positions.

DETERMINATION OF UNCERTAINTIES

There are two sources of error to consider: random error and systematic error. In our previous orbit determinations, the systematic error has in some cases dominated over the random error, which is why we treat them here separately.

Random error. Uncertainties in the various orbital elements were computed using a Monte Carlo approach. Fifteen additional data sets were synthesized by adding random Gaussian noise to the real data, using either 0.0024 arcsec (for the 54 observations away from minimum separation) or 0.0060 arcsec (for the 6 observations near mini-

mum separation) for the population standard deviation. The random errors were determined by computing the standard deviation of the resulting sixteen sets of orbital parameters.

Systematic error. The main source of systematic error differs from orbital element to orbital element. In the case of the semimajor axis, the accuracy of the image scale is the limiting instrumental factor. However, as noted earlier, we believe the systematic error in image scale is less than 2.6 km in the semimajor axis, but this determination does depend on the assumption that the image scale is constant to better than one part in ten thousand over time scales of several hours, which includes several day–night transitions for HST.

The eccentricity is quite sensitive to the particular albedo models adopted for Pluto and Charon, given that the eccentricity is so close to zero. Because of this model dependency, no useful quantitative limit can be placed on the systematic error in the eccentricity. Given that the center-of-body to center-of-light offset must be less than the radius of the body, we can say that the systematic error in eccentricity must be less than 0.09, which assumes a worst-case scenario of maximum (and unrealistic) offset on Pluto and Charon, with their respective offsets being in the opposite direction from one another. Because such offsets are not constrained to be in any particular direction, the potential systematic error in the longitude of periapsis could produce a value anywhere from 0° to 360°.

The systematic error in orbital inclination is controlled primarily by our knowledge of the offset between the V_3 axis and the columns of the P6 CCD chip. As mentioned in the calibration section, we estimate the systematic error to be less than 0.01°, which is smaller than our 0.032° random error.

The determination of the longitude of the ascending node relies primarily on the accuracy of the DE245 ephemeris for Pluto. Recent transit circle observations for Pluto indicate that the error in the DE211 ephemeris (upon which DE245 improves) is less than 0.5 arcsec (Standish 1994), which is much smaller than the random error in our ascending node determination, so once again we expect the random error to be dominant.

The systematic error in orbital period depends on the accuracy with which the time interval is measured over a span of 15 months. In the Appendix, note that we have accounted for the leap seconds that occurred during our observational period, so timing errors are presumably much less than 1 sec. Given the time span of 71 orbits for Charon, the systematic error in the period ought to be less than 10^{-8} days, which is about three orders of magnitude smaller than our random error.

Systematic error in the mean longitude is dominated by the error in the orbital period and the time interval between the arbitrarily chosen epoch of osculation and the mean time of the observations. In our case, the epoch was chosen to be close to the mean observation time (they differ by about six days), and the orbital period is known to a high degree of accuracy, so the systematic error is approximately 0.001°, which is more than an order of magnitude smaller than the random error. The value of the mean longitude is correlated with the inclination and ascending node, however, so even if the period and epoch were left unchanged, the mean longitude could still change in response to changes in these other parameters.

Note that in the discussion concerning the systematic error in the semimajor axis, the image scale was called the limiting *instrumental* factor. This distinction is important, given the last solution in Table III, which shows the semimajor axis to be rather sensitive to the particular albedo model adopted. Unfortunately, at this time we have no good way to determine how large the difference might be between our albedo models and the true surfaces of Pluto and Charon. Fortunately, the other elements (aside from the eccentricity) appear to be less sensitive to the albedo model.

MASS RATIO

Although our observations were not optimized for the determination of the Charon/Pluto mass ratio, some information is nevertheless present in the data. When we used the JPL DE245 ephemeris to compute the position of Pluto, what we were really computing was the location of the Pluto–Charon barycenter. Therefore the position on the CCD that we should have used in the image scale computation is the position of the Pluto–Charon barycenter. Given that the majority of Pluto's motion is in the east–west direction on the sky, while the majority of the barycenter's motion relative to Pluto is in the north–south direction, we did not expect our data to be particularly diagnostic of the mass ratio. Surprisingly, the result, as shown in Fig. 5, falls between two previous (and discrepant) results (Null *et al.* 1993, Young *et al.* 1994), though with a sufficiently large uncertainty to not favor either of those two determinations.

To arrive at this best-fit mass ratio, we simply noted the size of the scatter (as indicated by the reduced χ^2 statistic) in the image scale determinations based on the 22 pairs of exposures as a function of the assumed mass ratio. This technique explicitly assumes that the image scale is constant to about one part in ten thousand. A better approach would involve the inclusion of short-term variations in the image scale caused by thermal cycling; however, such an effort is beyond the scope of this paper. The result is a Charon/Pluto mass ratio of $0.110^{+0.063}_{-0.056}$, which can be compared with earlier published results of 0.084 ± 0.015 (Null *et al.* 1993) and 0.157 ± 0.004 (Young *et al.* 1994). Both of the earlier determinations are technically superior to

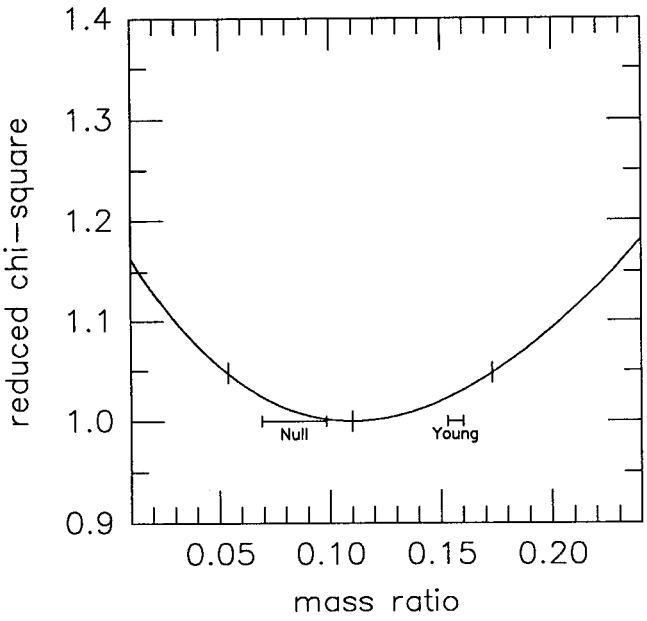

FIG. 5. Best-fit mass ratio. The reduced χ^2 statistic is plotted versus mass ratio in the sense Charon to Pluto. The value of the reduced χ^2 statistic is based on the scatter in 22 image scale determinations derived from the motion of the Pluto–Charon system relative to a field star on pairs of images taken several hours apart. The minimum occurs at a mass ratio of 0.110, which is marked by a short vertical bar. Vertical bars also indicate plus and minus one standard deviation, based on an increase in the value of χ^2 by one (or an increase of 0.048 in the reduced χ^2 for 21 degrees of freedom). Other mass ratio solutions from Null *et al.* (1993) and Young *et al.* (1994) are also indicated by horizontal bars that span plus and minus one standard deviation from their best-fit values.

ours, yet they disagree rather significantly, which is why we mention our result, despite its theoretically inferior pedigree.

DISCUSSION

Our orbit solution can be compared with earlier determinations. In Table IV, we have collected solutions based on direct imaging from Young *et al.* (1994), Null *et al.* (1993), and Beletic *et al.* (1989). In addition, we have included the latest solution based on mutual event data (Tholen and Buie 1990). The tabulated values shown in brackets were not free parameters in their respective orbit solutions, but rather were fixed at previously published or assumed values.

Our semimajor axis of 19,636 ± 8 km is in surprisingly good agreement with the earlier result from Beletic *et al.* (1989), despite the factor of 40 difference in the standard deviations. Although our result is significantly larger than the 19,405 ± 86 km and 19,460 ± 58 km results from Null *et al.* (1993) and Young *et al.* (1994), respectively, it should be noted that their results were constrained by assumed values of the eccentricity, the orbital period, and in one case the ascending node, all of which are improved upon in this work. When Null *et al.* performed an unconstrained solution for the semimajor axis, a much larger value and

TABLE IV

Orbit Solution Comparisons (Mean Equator and Equinox of J2000.0, Epoch JDT 2449000.5 = 1993 January 13.0 TT)

	this paper	Young *et al.* (1994)	Null *et al.* (1993)	mutual events	Beletic *et al.* (1989)
semimajor axis (km)	19636 ± 8	19460 ± 58	19405 ± 86	[19640]	19640 ± 320
eccentricity	0.0076 ± 0.0005	[0.0]	[0.0]	0.00020 ± 0.00021	[0.0]
inclination (deg)	96.163 ± 0.032	95.00 ± 0.24	96.56 ± 0.26	99.1 ± 1.0	98.5 ± 0.9
ascending node (deg)	222.993 ± 0.024	[223.01]	223.007 ± 0.041	223.015 ± 0.024	222.96 ± 0.21
long. periapsis (deg)	219.1 ± 2.2	—	—	73 ± 31	—
mean longitude (deg)	32.875 ± 0.047	[32.34]	32.58 ± 0.24	32.34 ± 0.25	32.96 ± 0.93
period (days)	6.387223 ± 0.000017	[6.387246]	[6.387246]	6.387246 ± 0.000011	6.387219 ± 0.000035

error bar of 19,498 ± 267 km were found, which makes their result formally consistent with our new result. A similarly unconstrained solution for the Young *et al.* data yielded 19,484 ± 64 km, however, which differs from our result by an uncomfortably large 2.4 standard deviations. Note that the Young *et al.* result is based on 19 observations from 1992 March 2, which falls fairly close to Charon's periapsis (q = 19,487 km), and only 6 observations from 1992 February 29, which comes the closest to Charon's apoapsis (but not as close as the March 2 data do to periapsis), so perhaps a combination of an assumed zero eccentricity, and the implicit weighting of data closer to where our observations show periapsis to be, resulted in a smaller fitted value for the semimajor axis.

An important implication of our new value for the semimajor axis is that it is not necessary to shrink the mutual-event-based radii of Pluto and Charon to satisfy a smaller semimajor axis; thus the discrepancy with the stellar occultation results is not as large as was previously suspected. In addition, with a better value for the orbital inclination provided by this work, the mutual event solution for the two radii can be constrained to use this better value. Although a new mutual event model is beyond the scope of this paper, we can note that previous solutions using a constrained lower value for the inclination produced slightly larger values for the radii. Young and Binzel (1994) have also noted the same effect, which for their solutions amounted to -3.9 km deg^{-1} and -5.2 km deg^{-1} for Pluto and Charon, respectively.

Using 19,636 ± 8 km for the semimajor axis, the radii of Pluto and Charon, respectively, as determined by Reinsch *et al.* (1994), would be 1151 ± 4 km and 591 ± 5 km, while Young and Binzel (1994) would find 1178 ± 23 km and 628 ± 21 km. The former results are in excellent agreement with our own (1151 ± 6 km and 593 ± 13 km, Tholen and Buie 1990), while the Young and Binzel radii are larger primarily because of their inclusion of limb darkening, which the other two solutions lack. Of course, none of these solutions incorporate the effects of the orbital eccentricity found in this work.

The biggest surprise was the size of the orbital eccentricity and the small formal error in that determination. Although an eccentricity of 0.0076 is much larger than we expected, it is formally consistent with the mutual event constraint, because as luck would have it, the line of apsides turns out to be nearly perfectly aligned with the direction to Earth (the mutual event value shown in Table IV constrained the line of apsides to not fall along the line of sight). With such an orientation, the well-determined time interval between consecutive mutual events remains equal, while the slight difference in the duration of inferior and superior events is masked by the uncertainties in the determinations of the radii for Pluto and Charon. With a longitude of periapsis of 219.1°, periapsis occurs with Charon behind Pluto, therefore Charon's orbital velocity was highest during the superior events and slowest during the inferior events. This effect will tend to shrink the Young and Binzel (1994) radius for Charon slightly, given that their result depends primarily on the inferior events, while slightly increasing the size of Pluto, whose radius determination depends on the superior events in their method.

We were also initially surprised that the eccentricity would go down to 0.0030 when the COB–COL offset for Pluto was incorporated into the orbit solution. After all, the albedo maps show bright regions in the southern hemisphere of Pluto (Buie *et al.* 1992), leading us to expect a southward shift in the center of light, which translates into a smaller distance between Charon's periapsis and Pluto's center of body, thereby increasing the eccentricity. Upon closer examination, however, although it is true that the southern hemisphere of Pluto has the brightest regions, it also has some of the darkest regions, and the average albedo of the less-contrastive northern hemisphere turned out to be slightly higher than for the southern hemisphere, thereby producing a northward shift in the center of light. Clearly more work is required to improve on the albedo maps of the system before a definitive value for the orbital eccentricity can be extracted from astrometric measurements.

That a tidally evolved system such as Pluto–Charon should have so large an eccentricity as 0.0030 is another surprise. Perhaps the system is still recovering from a recent impact that had disrupted synchronicity, a hypothesis that has rather important implications for the population density in the outer Solar System (Weissman *et al.* 1989). In this context, it is worth noting that through the end of 1995, 32 trans-Neptunian bodies have been discovered, some with orbits suggestive of 3:2 resonance with Neptune, just like Pluto (Marsden 1994). Weissman and Stern (1994) found that Kuiper belt comets dominate the impact rate on Pluto and Charon, compared with the inner Oort cloud, which contributes only 2 to 3% of the impact numbers; other sources contribute negligible impact rates. They estimated an average impact rate of one every 2 Myr for Pluto and one every 10 Myr for Charon. Assuming a value of 100 for the dissipation function Q, the time scale for eccentricity damping is about 10 Myr (Peale *et al.* 1980). On the other hand, if the ice mantle of a differentiated Pluto dominated the tidal dissipation, then Q might be as large as 1000, thereby increasing the time scale for eccentricity damping to 100 Myr. It would appear that the impact hypothesis for eccentricity excitation is reasonably consistent with these time scales and the population statistics assumed by Weissman and Stern, though a closer examination of the size–frequency distribution is in order, given that an impact by a fairly large body (tens of kilometers) is necessary to produce an eccentricity this large (Peale, personal communication).

Any impact energetic enough to excite an eccentricity of about 0.0030 ought to leave a rather significant scar on the surface of the target. In this connection, it is worth noting that we have no other good explanation for the dark region on Pluto that produces minimum light in the rotational lightcurve, or alternatively, the bright region that produces lightcurve maximum. The large-scale surface contrast on Pluto is second only to that of Iapetus in the Solar System, but there is an obvious mechanism for the contrast on Iapetus, given its tidal locking with Saturn and the in-falling material hypothesis (Cook and Franklin 1970, Cruikshank *et al.* 1983). We speculate that this dark region on Pluto may be the result of surface contamination by an impacting body, or alternatively, the bright region could be the result of excavation of fresh subsurface icy material by an impact.

An impact capable of exciting a nonzero orbital eccentricity could also produce a nonzero orbital inclination relative to the equator of Pluto. Although the damping of Charon's relative inclination occurs much more rapidly than the circularization of the orbit (Dobrovolskis, personal communication), we cannot rule out the possibility of a nonzero relative inclination, if the hypothesized impact occurred sufficiently recently, which calls into question yet another often-made assumption about the system.

Although others performing orbit solutions have attempted to solve for the eccentricity, they have always found the result to be indistinguishable from zero and therefore simply adopted zero for the eccentricity, partly because of the expectation based on the complete tidal evolution of the system. However, it is interesting to note that the Null *et al.* (1993) unconstrained result yielded 0.007 ± 0.011 for the eccentricity, which looks surprisingly similar to our uniform-albedo-based value. Null *et al.* did not include a value for the longitude of periapsis, however, so a formal comparison with that result can not be made.

Our orbital inclination result lies between the Null *et al.* (1993) and Young *et al.* (1994) determinations. If the error bars are taken at face value, then none of the results agree to better than 1.5 standard deviations, which is somewhat disturbing. Even the mutual event result and the Beletic *et al.* (1989) value show error bars that are significantly smaller than their differences from our new result. (Note that before a direct comparison can be made, all results need to be referred to the same reference frame. As published, the mutual event and Beletic *et al.* inclinations are based on the B1950.0 reference frame, while the others mentioned here were published using the J2000.0 frame. We performed the rotation on the B1950.0 results before inclusion in Table IV.) Of all the orbital elements derived from the mutual event observations, however, the orbital inclination is the most poorly constrained. The published error bar of 1.0° reflects only the formal error multiplied by an arbitrary factor intended to account for possible systematic error and correlations with other fitted parameters; thus a formal comparison is not strictly valid. The Null *et al.* and Young *et al.* values were calibrated using the motion of Pluto itself, which is known quite well, so these discrepancies are more disturbing. The Beletic *et al.* value was calibrated using the trailed image of a field star made with the telescope drive turned off, therefore the trail represents the direction of true east–west extremely well and was determined to better than 0.4° accuracy (which is much less than the random error), so once again the 2.7σ difference between the two inclinations is disturbing. We can offer no reasonable explanation for these differences at this time.

The longitude of the ascending node is quite consistent with the other determinations presented here. Unlike the inclination, the ascending node is one of the best-determined elements from the analysis of mutual event data, and none of the direct imaging results is formally superior to the mutual event result, though the same caveat about the error bar on the mutual-event-based inclination applies to the ascending node as well.

The orbital period was not determined by either Null *et al.* (1993) or Young *et al.* (1994), due to the short timebase for their observations. Because our HST data span 15 months, we are able to derive an orbital period independently. The result is 6.387223 ± 0.000017 days, which is formally consistent with the mutual event result of 6.387246 ± 0.000011 days, which is based on data that span six years (Tholen and Buie 1990). The Beletic *et al.* (1989) value for the period is based on a combination of speckle data that span one year and three years of mutual event data, so the agreement with our new value is not unexpected.

Part of the evidence for the Pluto–Charon system being tidally evolved comes from the agreement between the orbital period for Charon (6.387223 ± 0.000017 days) and the rotational period for Pluto (6.38726 ± 0.00007 days). The latter result is based on lightcurve studies of the system (Tholen and Tedesco 1994), which make the implicit assumption that there are no longitudinal shifts in the locations of lightcurve features as a function of sub-Earth latitude. For example, suppose Pluto had a dark stripe oriented at an angle relative to its equator on an otherwise uniform surface. As the sub-Earth latitude traveled from south to north of the equator, the longitude corresponding to minimum light would shift, and the resulting lightcurve period would not represent the rotational period of the planet. We believe that this is why Lyutyi and Tarashchuk (1984) derived a slightly shorter lightcurve period for the system (6.38663 ± 0.00006 days), given that they used lightcurve data from as far back as 1953, despite the obvious change in lightcurve amplitude with time. As such, the comparison of orbital period with rotational period ought to be done using the more limited range

of sub-Earth latitudes represented by the Tholen and Tedesco data.

The accompanying paper (Buie *et al.* 1997) demonstrates that the lightcurve of Charon is consistent with a synchronous rotational period, which is to be expected, given that the locking of the secondary body's rotation occurs much more quickly than that of the primary's (Farinella *et al.* 1979), but now we have our first observational evidence for that expected result.

These values for the semimajor axis and orbital period imply a system GM of 981.5 ± 1.1 km^3 sec^{-2}, which leads to a Sun/Pluto–Charon mass ratio of 135,220,000 ± 160,000. These results will be useful to those performing numerical integrations of the Solar System, who have had a comparatively poor value of the system mass to use previously.

FUTURE WORK

The most pressing need at the moment is to verify the existence of the eccentricity found in these observations. With the refurbished HST, the problem we encountered in determining the centroids near minimum separation will be greatly reduced by the virtual elimination of the spherical aberration. In addition, the minimum separation distance will continue to increase as the sub-Earth latitude continues its northward trek, making it even easier to obtain those critical measurements near minimum separation. With the line of apsides lying along the line of sight from Earth, the highest and lowest orbital velocities will occur when Charon is at minimum separation.

Direct imaging with HST can resolve the disk of Pluto, permitting actual measurements of the offset in the center of light from the center of body, thereby eliminating the need to rely on models of the surface albedo distribution as we have done here. Doing the same for Charon represents more of a problem, however, given that it subtends only about two pixels when using the Faint Object Camera.

We also plan to combine these measurements with those of Null *et al.* (1993) and Young *et al.* (1994) in an attempt to produce an even better orbit solution, assuming that we can convince ourselves that there are no significant systematic differences in the image scale or position angle calibrations for these three data sets (as suggested by the discrepant orbital inclination results). It may even be of some value to include the lower quality speckle observations from Beletic *et al.* (1989) because they increase the timebase significantly, thereby allowing an even better orbital period to be extracted from the data.

Once definitive orbital parameters have been determined, a new analysis of the mutual event data can be performed, with constraints applied to the orbit where appropriate. Such an analysis ought to yield the most reliable solutions for the individual radii of the two bodies. When coupled with the individual masses determined from the barycentric wobble observations, the individual densities can at last be computed with some confidence.

Lastly, it is now clear that we have reached the limit of orbit solution accuracy using only astrometric data that provide the separation and position angle. Future improvements in the orbit solution for Charon, particularly the eccentricity, must account for the albedo features on Pluto and Charon, thus additional improvements in the albedo maps are a necessary prerequisite.

APPENDIX

Because of the discrepancies between the various published orbital parameters for the Pluto–Charon system, we thought it would be useful to provide a more detailed account of the procedure we used to compute our orbit for Charon. Because the orbital elements were determined by minimizing the sum of squares of the residuals between the observed and computed positions of Charon relative to Pluto, the following steps are divided into those used to arrive at the computed position and those used to arrive at the observed position, followed by a description of the orbit solution itself.

Computed position.

1. We started with the UTC midtimes of the HST observations, given to a precision of 10^{-8} day, but rounded these numbers to the nearest 10^{-7} day.

2. The UTC times were input to a program that computed the position of the spacecraft in the J2000.0 frame for the particular instant of time. The source for the spacecraft ephemeris was a set of files, each covering two days, with the position and velocity vectors tabulated at one minute intervals, as provided by STScI. The entry closest in time to the observation midtime was extracted, converted into a set of classical elliptical orbital elements, and the spacecraft position for the exact time was then computed assuming two-body motion. In computing the orbit of the spacecraft, the mass of the Earth was calculated from DE245 to be 3.00349×10^{-6} solar masses. This procedure ignores any irregularities in the Earth's gravity field traversed by the spacecraft during the maximum of 30 sec between our observation midtime and the nearest entry in the spacecraft ephemeris file, but is more than adequate for our purposes. The error in the spacecraft position is guaranteed to be less than 200 m at each epoch in the ephemeris file (and in fact averaged only 71 m in 1993), while the error in the spacecraft velocity is less than 15 cm sec^{-1}.

3. The spacecraft position vector, expressed in kilometers, was converted to astronomical units using the DE245 value of 149,597,870.7 km AU^{-1}.

4. The UTC observation midtimes were converted to the TDT reference frame using ΔTT (= TDT − UTC)

values of 58.184 sec prior to 1992 July 1, 59.184 sec between 1992 July 1 and 1993 July 1, and 60.184 sec after 1993 July 1.

5. The TDT times were input to another program that computed the heliocentric positions of the Earth and the Pluto–Charon barycenter in the J2000.0 frame using DE245. The Earth and spacecraft vectors were added, and the result was then subtracted from the heliocentric Pluto–Charon barycenter vector to produce a topocentric vector to the Pluto–Charon barycenter. The light travel time was computed, subtracted from the observation time, and used to recompute the Pluto–Charon barycenter ephemeris position. This step was repeated until it converged to a precision of 10^{-9} AU. To compute the light travel time, 299,792.458 km sec^{-1} was used for the speed of light, and the conversion from kilometers to astronomical units utilized the value given in step 3 above.

6. Given a starting set of J2000.0 orbital elements for Charon, we computed the Pluto to Charon vector in the J2000.0 frame for each of the lighttime-corrected times. Two-body motion of Charon around Pluto was assumed, and the difference in light travel time to Pluto and Charon (less than 7.6×10^{-7} day) was ignored.

7. We rotated that vector from the J2000.0 reference frame into a coordinate system aligned with the plane of the sky using the J2000.0 right ascension and declination for the Pluto–Charon barycenter derived from DE245. The rotated positive x axis points toward J2000.0 north on the sky, the positive y axis points toward east on the sky, and the positive z axis, as required by the right-hand rule, points toward the observer.

8. Using the topocentric distance of the Pluto–Charon barycenter derived from DE245, the position vector of Charon relative to Pluto, as projected onto the plane of the sky, was converted from kilometers to arcseconds.

Observed position.

1. To generate the observed separation and position angle of Charon from Pluto, we first processed the raw images with the CLEAN algorithm to reduce the effects of spherical aberration on the images. This algorithm was chosen because it conserves photons, and relative photometry was another goal of the observations.

2. The CLEANed images were convolved with a Gaussian image profile to impose a well-behaved point spread function on the reconstructed image.

3. Image centroids for Pluto, Charon, and the field star were computed using the center-of-light method.

4. These centroids were processed by the METRIC software package in STSDAS to correct for field distortion.

5. Using the DE245 ephemeris to provide the direction and amount of motion for the Pluto–Charon system between pairs of frames that show the same field star, the image scale and position angle offset were computed, as described more thoroughly in the main part of the paper. Note in particular that these calculations were done on the distortion-corrected images, not the raw images, so in theory the image scale and position angle of J2000.0 north should be uniform across the images.

6. Pixel coordinates were rotated into a frame that aligns the axes with J2000.0 north and east using the roll angle and offset, and then converted into arcseconds using the image scale.

Orbit solution.

1. Using a weighted, nonlinear least-squares approach, the differences between the computed and observed positions of Charon on the plane of the sky were then minimized by allowing the seven orbital parameters (a, i, Ω, L, P, $e \cos \tilde{\omega}$, and $e \sin \tilde{\omega}$) to vary. The weights were computed using the inverse square of the assigned uncertainties, as indicated in the main text.

2. To guard against the possibility of the orbit solution settling into a local minimum rather than an absolute minimum, the solution process was performed using several different sets of starting elements. All converged to the same final set of orbital elements.

3. Fifteen additional synthetic data sets were generated by adding Gaussian noise to the original data set. An orbit solution was performed on each of these, and the resulting standard deviation in each orbital element was used to represent the random error in that element.

4. Center-of-body to center-of-light offsets were computed for both Pluto and Charon using models of the surface albedo distribution from Buie *et al.* (1992). These were used to estimate the effect of albedo on the orbit solution.

ACKNOWLEDGMENTS

We thank the following people at the Space Telescope Science Institute for their assistance: Jonathan Eisenhamer handled our request for the HST ephemeris, Daniel Golombek provided information about the HST spacecraft ephemeris uncertainty and time scale, and Alex Storrs cheerfully provided answers to additional questions about HST. E. Myles Standish provided access to the JPL DE245 ephemeris, and Faith McCreary answered our questions about the code used to generate the ephemeris data. The research benefited from useful discussions with Stan Peale, Gene Shoemaker, and Tony Dobrovolskis. Improvements to the manuscript resulted from excellent reviews by Alan Stern and an anonymous referee. In particular, the latter made a recommendation that enabled us to improve on the STScI value for the position angle offset. Support for this work was provided by NASA through Grant GO-03848.01-91A from the Space Telescope Science Institute, which is operated by the Association of Universities for Research in Astronomy, Inc., under NASA Contract NAS5-26555. The first author also acknowledges support from NASA Grants NAGW 1991 and NAGW 3093.

REFERENCES

BAIER, G., AND G. WEIGELT 1987. Speckle interferometric observations of Pluto and its moon Charon on seven different nights. *Astron. Astrophys.* **174,** 295–298.

BELETIC, J. W., R. M. GOODY, AND D. J. THOLEN 1989. Orbital elements of Charon from speckle interferometry. *Icarus* **79,** 38–46.

BONNEAU, D., AND R. FOY 1980. Speckle interferometry with the CFHT 3.60 m. I. Resolution of the system Pluto–Charon. *Astron. Astrophys.* **92,** L1–L4.

BUIE, M. W., AND S. J. BUS 1992. Physical observations of (5145) Pholus. *Icarus* **100,** 288–294.

BUIE, M. W., D. J. THOLEN, AND K. HORNE 1992. Albedo maps of Pluto and Charon: Initial mutual event results. *Icarus* **97,** 211–227.

BUIE, M. W., D. J. THOLEN, AND L. H. WASSERMAN 1997. Separate lightcurves of Pluto and Charon. *Icarus* **125,** 233–244.

CHRISTY, J. W., AND R. S. HARRINGTON 1978. The satellite of Pluto. *Astron. J.* **83,** 1005–1008.

COOK, A. F., AND F. A. FRANKLIN 1970. An explanation of the light curve of Iapetus. *Icarus* **13,** 282–291.

CRUIKSHANK, D. P., J. F. BELL, M. J. GAFFEY, R. H. BROWN, R. HOWELL, C. BEERMAN, AND M. ROGNSTAD 1983. The dark side of Iapetus. *Icarus* **53,** 90–104.

ELLIOT, J. L., AND L. A. YOUNG 1991. Limits on the radius and a possible atmosphere of Charon from its 1980 stellar occultation. *Icarus* **89,** 244–254.

FARINELLA, P., A. MILANI, A. M. NOBILI, AND G. B. VALSECCHI 1979. Tidal evolution and the Pluto–Charon system. *Moon Planets* **20,** 415–421.

HARRINGTON, R. S., AND J. W. CHRISTY 1980. The satellite of Pluto. II. *Astron. J.* **85,** 168–170.

HARRINGTON, R. S., AND J. W. CHRISTY 1981. The satellite of Pluto. III. *Astron. J.* **86,** 442–443.

HEGE, E. K., AND J. DRUMMOND 1984. IAU Circular 3986.

HEGE, E. K., E. N. HUBBARD, J. D. DRUMMOND, P. A. STRITTMATTER, S. P. WORDEN, AND T. LAUER 1982. Speckle interferometric observations of Pluto and Charon. *Icarus* **50,** 72–81.

HETTERICH, N., AND G. WEIGELT 1983. Speckle interferometry observations of Pluto's moon Charon. *Astron. Astrophys.* **125,** 246–248.

LYUTYI, V. M., AND V. P. TARASHCHUK 1984. A photometric study of Pluto near perihelion. II. Rotation period and color indices. *Sov. Astron. Lett.* **10,** 226–229.

MARSDEN, B. G. 1994. IAU Circulars 6076 and 6085.

MILLIS, R. L., L. H. WASSERMAN, O. G. FRANZ, R. A. NYE, J. L. ELLIOT, E. W. DUNHAM, A. S. BOSH, L. A. YOUNG, S. M. SLIVAN, A. C. GILMORE, P. M. KILMARTIN, W. H. ALLEN, R. D. WATSON, S. W. DIETERS, K. M. HILL, A. B. GILES, G. BLOW, J. PRIESTLEY, W. M. KISSLING, W. S. G. WALKER, B. F. MARINO, D. G. DIX, A. A. PAGE, J. E. ROSS, H. P. AVEY, D. HICKEY, H. D. KENNEDY, K. A. MOTTRAM, G. MOYLAND, T. MURPHY, C. C. DAHN, AND A. R. KLEMOLA 1993. Pluto's radius and atmosphere: Results from the entire 9 June 1988 occultation data set. *Icarus* **105,** 282–297.

NULL, G. W., W. M. OWEN JR., AND S. P. SYNNOTT 1993. Masses and densities of Pluto and Charon. *Astron. J.* **105,** 2319–2335.

PEALE, S. J., P. CASSEN, AND R. T. REYNOLDS 1980. Tidal dissipation, orbital evolution, and the nature of Saturn's inner satellites. *Icarus* **43,** 65–72.

REINSCH, K., V. BURWITZ, AND M. C. FESTOU 1994. Albedo maps of Pluto and improved physical parameters of the Pluto–Charon system. *Icarus* **108,** 209–218.

RUSSELL, J. L., B. M. LASKER, B. J. MCLEAN, C. R. STURCH, AND H. JENKNER 1990. The Guide Star Catalog. II. Photometric and astrometric models and solutions. *Astron. J.* **99,** 2059–2081.

SMITH, J. C. 1978. IAU Circular 3241.

STANDISH, E. M. 1994. Improved ephemerides of Pluto. *Icarus* **108,** 180–185.

THOLEN, D. J. 1985. The orbit of Pluto's satellite. *Astron. J.* **90,** 2353–2359.

THOLEN, D. J., AND M. W. BUIE 1988. Circumstances for Pluto–Charon mutual events in 1989. *Astron. J.* **96,** 1977–1982.

THOLEN, D. J., AND M. W. BUIE 1989. Further analysis of Pluto–Charon mutual event observations—1989. *Bull. Am. Astron. Soc.* **21,** 981–982.

THOLEN, D. J., AND M. W. BUIE 1990. Further analysis of Pluto–Charon mutual event observations—1990. *Bull. Am. Astron. Soc.* **22,** 1129.

THOLEN, D. J., AND E. F. TEDESCO 1994. Pluto's lightcurve: Results from four oppositions. *Icarus* **108,** 200–208.

WALKER, A. R. 1980. An occultation by Charon. *Mon. Not. R. Astron. Soc.* **192,** 47P–50P.

WEISSMAN, P. R., A. R. DOBROVOLSKIS, AND S. A. STERN 1989. Constraints on impact rates in the Pluto–Charon system and the population of the Kuiper comet belt. *Geophys. Res. Lett.* **16,** 1241–1244.

WEISSMAN, P. R., AND S. A. STERN 1994. The impactor flux in the Pluto–Charon system. *Icarus* **111,** 378–386.

YOUNG, E. F., AND R. P. BINZEL 1993. Comparative mapping of Pluto's sub-Charon hemisphere: Three least squares models based on mutual event lightcurves. *Icarus* **102,** 134–149.

YOUNG, E. F., AND R. P. BINZEL 1994. A new determination of radii and limb parameters for Pluto and Charon from mutual event lightcurves. *Icarus* **108,** 219–224.

YOUNG, L. A., C. B. OLKIN, J. L. ELLIOT, D. J. THOLEN, AND M. W. BUIE 1994. The Charon–Pluto mass ratio from MKO astrometry. *Icarus* **108,** 186–199.